ASME'93

Selected Computations of Transonic Cavity Flows

Christopher A. Atwood
MCAT Institute
NASA Ames Research Center
Moffett Field, CA 94035-1000

1993 ASME Fluids Engineering Conference
Forum on Computational Aero- and Hydro-Acoustics
June 20-24, 1993/Washington D.C.

SELECTED COMPUTATIONS OF TRANSONIC CAVITY FLOWS

Christopher A. Atwood
MCAT Institute, NASA Ames Research Center
Moffett Field, California 94035-1000

ABSTRACT

An efficient diagonal scheme implemented in an overset mesh framework has permitted the analysis of geometrically complex cavity flows via the Reynolds-averaged Navier-Stokes equations. Use of rapid hyperbolic and algebraic grid methods has allowed simple specification of critical turbulent regions with an algebraic turbulence model. Comparisons between numerical and experimental results are made in two-dimensions for the problems of: a backward-facing step, a resonating cavity, and two quieted cavity configurations. In three-dimensions, the flow about three early concepts of the Stratospheric Observatory For Infrared Astronomy (SOFIA) are compared to wind-tunnel data. Shedding frequencies of resolved shear layer structures are compared against experiment for the quieted cavities. The results demonstrate the progress of computational assessment of configuration safety and performance.

NOMENCLATURE

c	speed of sound
C_p	coefficient of pressure, $\frac{p-p_\infty}{q_\infty}$
f	frequency
K	ratio of convection by freestream speed
ℓ	mixing length
L	characteristic length
m	stage number
$\dot{m}$	mass flow rate
M	Mach number
p	instantaneous static pressure
PSD	power spectral density, dB
q	velocity magnitude or dynamic pressure
Q	vector of dependent variables
r	velocity ratio, $\frac{u_1}{u_2}$
Re	Reynolds number
St	Strouhal number, $\frac{f\theta}{u_1+u_2}$
SPL	sound power level, dB
t	time
u, v, w	Cartesian velocity components
x, y, z	Cartesian physical space coordinates
α	angle of attack
θ	momentum thickness
λ	wavelength
μ_t	eddy viscosity
ρ	density
σ	spreading rate parameter
$\overline{(\ )}$	mean quantity
$< >$	root mean square quantity
$(\ )'$	fluctuating quantity, $f = \overline{f} + f'$

Subscripts

a	acoustic
T	total quantity
v	vortical
∞	freestream quantity

INTRODUCTION

The effort reported here describes the progress of a computational approach for use in the design of a new airborne astronomical observatory. The existing Kuiper Airborne Observatory (KAO) has provided two decades of unique research capabilities.[1] Figure 1 depicts the proposed successor, SOFIA, which will offer

ten times more resolution than the KAO. Assessment of the safety and performance of this large cavity in a Boeing 747SP is the goal of this continuing effort. Towards this objective of providing design information, extensive evaluation of the numerical methods by comparison against experiment is necessary.

This report describes the status of the validation of the computational methods to date. In order to provide a somewhat complete overview, both previously reported[2] and new results are incorporated herein. The two-dimensional cases discussed here include free shear layers,[3] a backward-facing step,[4] a resonating cavity,[5] and two quieted cavities.[6] The computed three-dimensional cases are compared to the wind tunnel data of Rose and Cooley.[7] The following sections address the method used to predict the unsteady flows, including the grid generation and modelling of turbulence.

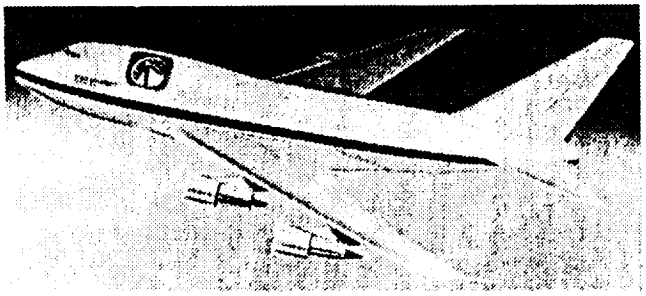

Fig. 1: An early conceptualization of SOFIA

METHOD

The fluid field was computed via the Navier-Stokes equations using the diagonal scheme of Pulliam and Chaussee[8] implemented in the overset grid framework of Benek, Buning, and Steger.[9] The equations were integrated through Euler implicit time marching and second-order spatial differencing with viscous wall conditions specified as no-slip, zero normal pressure gradient, and adiabatic. Information transfer across overset mesh boundaries was implemented using trilinear interpolation of the dependent variable vector, $Q = [\rho, \rho u, \rho v, \rho w, e]^T$. Computations were performed on the NAS Cray 2 and Y-MP, the CCF Cray Y-MP, and a Silicon Graphics 4D35TG workstation. The flow solver cost is $13\mu s$/cell/step on a Cray Y-MP.

Turbulence Model

In these computations, the slowly time-varying component of the flow is resolved, while rapid fluctuations are modelled. The algebraic turbulence model of Baldwin and Lomax,[10] as implemented by Buning,[11] is described below using a flow in the (x, y) plane.

The wall-bounded flows use the original Baldwin-Lomax model, with the addition of a variable F_{max} cutoff. The grids are chosen such that a unique wall distance is readily available.

The cavity aperture spanning shear layer uses an eddy viscosity developed using $F(y) = y|\omega|$, as suggested by Baldwin and Lomax[10] for wake regions. This results in

$$\begin{aligned} F_{wake} &= C_{wk}\frac{y_{max}u_{dif}^2}{F_{max}} \\ &= C_{wk}\left(\frac{u_{dif}}{|\omega|_{max}}\right)^2|\omega|_{max} \\ &\propto \ell^2|\omega| \end{aligned}$$

where specification of C_{wk} is discussed below and the velocity difference is modified to be half the total velocity difference between the streams in the specified shear layer region

$$u_{dif} = \sqrt{(u^2+v^2)}_{max} - \sqrt{(u^2+v^2)}_{|\omega|_{max}}$$

The free shear layer model is now given by

$$\mu_t = \rho K C_{cp} C_{wk} \frac{u_{dif}^2}{|\omega|_{max}} \qquad (1)$$

after dropping the Klebanoff intermittency function. Unmodified model constants $K = 0.0168$ and $C_{cp} = 1.6$ are used.

The magnitude of the eddy viscosity in the free shear layer model can be altered with C_{wk}. Estimation of the proper value of C_{wk} begins by using Görtler's shear layer solution:

$$u = \frac{u_1+u_2}{2}\left[1 + \frac{u_2-u_1}{u_2+u_1}erf(\xi)\right]$$

$$erf(\xi) = \frac{2}{\sqrt{\pi}}\int_0^x e^{-\xi^2}d\xi, \ \xi = \frac{\sigma y}{x}$$

where u_1 and u_2 are the velocities of the slow and fast streams and ξ is the similarity coordinate, as shown in Fig. 2. The spreading parameter σ is inversely related to the spreading rate, db/dx, where b is a measure of the shear layer width. The value of the spreading parameter when the velocity of one of the streams is zero is σ_0.

Görtler's solution can be used to determine the maximum vorticity magnitude as follows:

$$|\omega| = \left|\frac{\partial u}{\partial y}\right| = \left|\frac{\partial u}{\partial \xi}\frac{\partial \xi}{\partial y}\right|$$

$$= \left| \frac{\sigma}{x\sqrt{\pi}} \Delta u e^{-\xi^2} \right|, \Delta u = (u_2 - u_1)$$

$$|\omega|_{max} = \frac{\sigma}{x\sqrt{\pi}} \Delta u$$

Now, using Prandtl's mixing length assumption and scaling laws for jet boundaries, eddy viscosity can also be expressed as

$$\begin{aligned} \mu_t &\propto \rho \ell^2 |\omega| \\ &\propto \rho \ell^2 \frac{\Delta u}{b} \\ &= K_0 \rho b \Delta u \end{aligned} \quad (2)$$

where $K_0 = \frac{x}{4b\sigma_0^2}$.

Setting Eqs. 1 and 2 equal results in

$$C_{wk} = (\sigma_0 K C_{cp} \sqrt{\pi})^{-1}$$

and only σ_0 remains to be specified. Empirical estimates of σ_0 range from 9.0 to 13.5.[3, 12, 13] For this series of cavity flow efforts σ_0 was set to 11.0, resulting in a value of $C_{wk} = 1.91$.

Grid Generation

Computation of the loads generated by cavity flows requires accurate representation of the geometry as well as the flowfield. Typically, a significant effort in grid generation is required before flow analysis can begin. Since matching zone faces are not required for the overset method used here, recent advances in algebraic[15] and hyperbolic[14] methods can be used. Hyperbolic grid generation, which gives good spacing and orthogonality control, was used for the wall-bounded regions, while algebraic grids were used in shear flow regions including plumes and wakes. Advantages of this type of grid system include straightforward specification of the turbulent regions and allowance for independent refinement of each zone. This topology also permits the re-use of meshes for configuration studies.

FREE SHEAR LAYER

Numerical experiments were performed using a two-dimensional shear layer to determine sensitivities of mean and time-varying quantities to changes in time step size, fourth-order dissipation levels, and grid refinement. In addition, the algebraic turbulent shear layer model was partially validated through comparison with similarity solutions and experimental data.

The computational domain for this case is shown to scale in Fig. 2a, where inviscid channel side walls and characteristic inflow and outflow boundary conditions were used. The boundary layers on the splitter plate

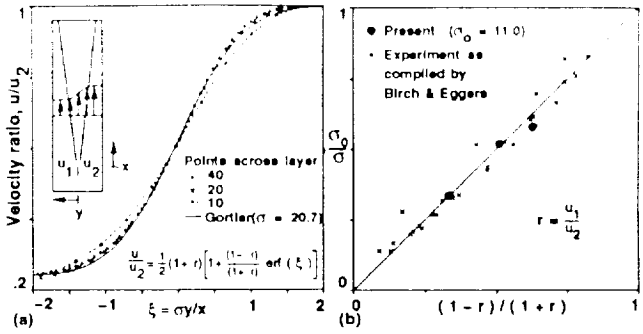

Fig. 2: Shear layer case: (a) velocity profiles of differing grid resolution compared to similarity and (b) variation of spread rate with velocity parameter

and the shear layer were fully turbulent with a Reynolds number based on the mean velocity of the streams and the length of the splitter plate given as 6.7×10^5.

The results for three grid refinement levels are also shown in Fig. 2a along with Görtler's similarity solution, where the velocity profiles were taken more than a thousand momentum thicknesses downstream of the trailing edge of the plate. The solution can be seen to become grid dependent when fewer than than 20 points span the layer. Eddy viscosity was observed to grow linearly in accordance with the Clauser formulation, while the solution was insensitive to fourth-order dissipation levels within the range 0.01 to 0.05. The Mach ratio for this case was 0.2/0.8 with $\sigma = 20.7$.

Figure 2b compares the variation of spread rate with velocity ratio, and demonstrates that computed spreading rates are within the bounds of the experimental data.

BACKWARD-FACING STEP

A qualitative estimate of the errors to be expected in the three-dimensional flows can be gleaned from the backward-facing step problem. The computation was compared to the experimental data of Driver and Seegmiller,[4] with test conditions matched at

$$M_{ref} = 0.128, \qquad Re_H = 3.44 \times 10^4$$
$$\rho_{ref} = 1.10\ kg/m^3, \quad p_{ref} = 9.11 \times 10^4\ N/m^2$$

Characteristic inflow and outflow boundaries were used, holding mass flow, total enthalpy, and flow angle fixed at the inlet while specifying pressure at the outlet. Both $\dot{m}$ and p_{exit} were iteratively adjusted to match two experimental conditions. First the overall pressure rise from $x/H = -4$ to $x/H = 30$ was matched to experiment, then $\dot{m}$ was modified to match the experimental momentum thickness at $x/H = -4$. Finally, viscous

adiabatic walls were specified for both the top and bottom of the channel. The unusual topology shown in Fig. 3 was used to replicate those required by the more complex configurations.

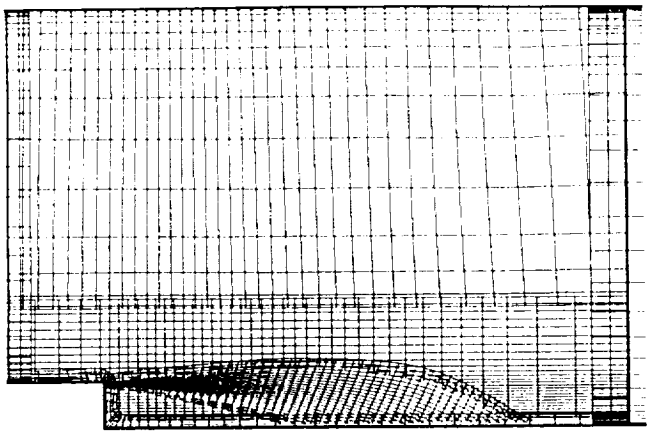

Fig. 3: Backward-facing step: coarsened near field grids

After dissipation of initial transients, the simulation, which was performed using a step size of $45\mu s$, was averaged over 200 steps by increments of 20 steps. Using a particle convecting with the shear layer from separation to the reattachment point, then 200 steps corresponds to three characteristic time increments. The time mean field was sampled in $H/10$ increments via trilinear interpolation of a valid donor cell to obtain the profiles shown in Fig. 4.

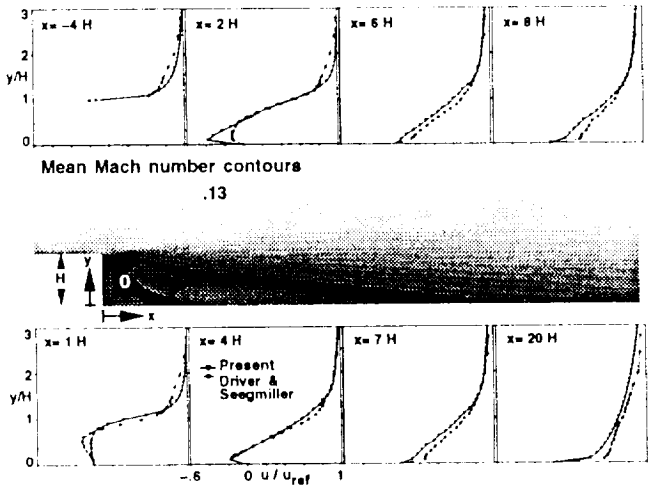

Fig. 4: Backward-facing step: velocity profiles

Agreement in maximum vorticity is seen in Fig. 4, however some discrepancies in profile shape exist. Using time mean skin-friction levels, the predicted reattachment occurred at $x/H = 6.3$ while experimental data showed reattachment at $x/H = 6.0$.

TWO-DIMENSIONAL RESONATING CAVITY

In order to establish confidence in the numerical method, a two-dimensional cavity computation was undertaken to demonstrate and validate[5] self-induced cavity resonance.

The test conditions, specified to match experiment, were

$$M_\infty = 0.9, \qquad Re_L = 1.47 \times 10^6, \qquad L = 8\ in.$$
$$\rho_\infty = 0.40\ kg/m^3, \quad p_\infty = 2.9 \times 10^4\ N/m^2$$

and a cavity length by depth, L/D, of 2. Characteristic inflow and outflow conditions were specified along with a step size of $\Delta t = 1.97\mu s$. Power spectra were computed using 8192 steps following the dissipation of the initial transients.

Inspection of the computed cavity pressure history, shown in Fig. 5a, confirms the idealized feedback mech-

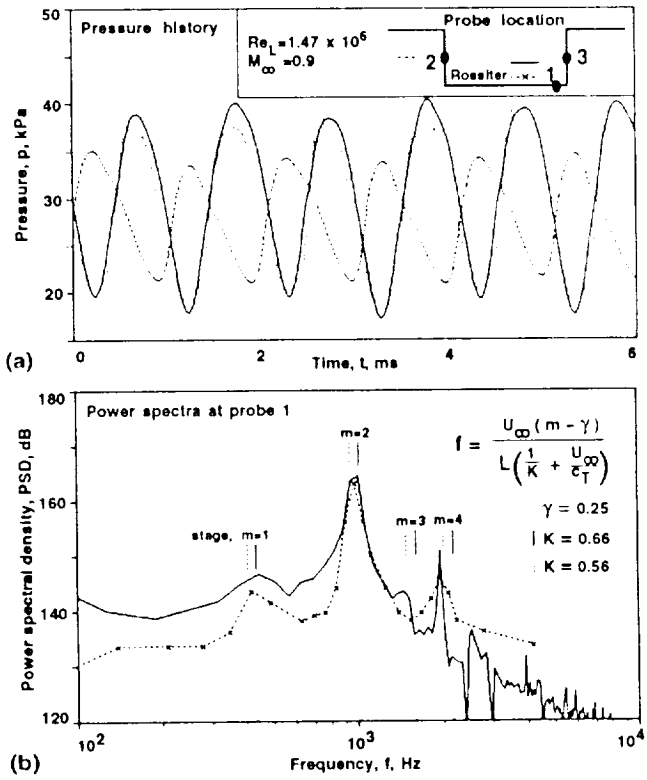

Fig. 5: 2-d cavity: (a) pressure history and (b) power spectra comparison

anism identified from Rossiter's experiments. Briefly, the cycle begins with the propagation of an acoustic wave from the aft wall of the cavity to the forward bulkhead. Wave reflection from the forward wall causes the

shear layer to bow outwards, shedding vorticity. The deflected shear layer convects downstream and induces another cycle. This coupling of the acoustic and vortical fields is quantified by Rossiter's empirical model, given in Fig. 5b, which gives only feedback frequencies.

In the frequency domain, comparison of Rossiter's data to present results indicate agreement in frequency at the peak magnitudes, as shown in Fig. 5b. Magnitudes are higher for the present case by about 2 dB, which can be explained from dimensionality arguments. The solution was also found to be insensitive to second-order dissipation levels within the range 0.3 to 0.5. Figure 5b also shows the resonant modes predicted by Rossiter's equation, showing that $K = 0.56$ gives better prediction of the higher modes. Finally, the vertical knife edge schlieren images of Fig. 6 show the qualitative agreement between computed and observed[16] radiation patterns.

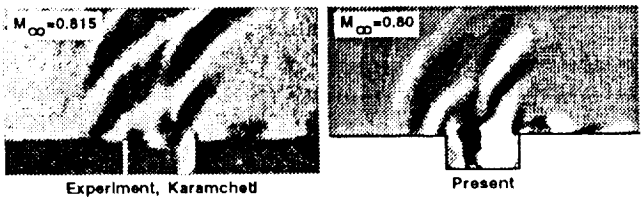

Fig. 6: Comparison of experimental and numerical schlieren images with knife edge vertical

TWO-DIMENSIONAL TREATED CAVITY

The effect of cavity geometry, particularly modification of the shear layer attachment region, is known to possess potential quieting capabilities.[17] The Army Airborne Optical Adjunct (AOA), shown in Fig. 7, flight tested several passive and active quieting methods.[6, 18] The purpose of the present numerical simulations is to determine if optical quieting methods, particularly aft ramp treatment and lip-blowing, could be accurately simulated.

The grid cell size was specified as 0.83 *in.* in the streamwise direction, chosen so that frequencies up to approximately 400 Hz would be resolved without significant numerical dissipation effects.[19] A time step of $44\mu s$ was fixed so that $CFL \approx 1$ in the streamwise direction within the shear layer. The numerical test conditions were matched to flight data:

$$M_\infty = 0.77, \qquad Re_L = 5.00 \times 10^6$$
$$\rho_\infty = 0.262\ kg/m^3, \quad p_\infty = 1.63 \times 10^4\ N/m^2$$

and $L = 47\ in.$ The initial conditions used the assumption of isentropic recovery to obtain the cavity temperature while maintaining constant pressure across the

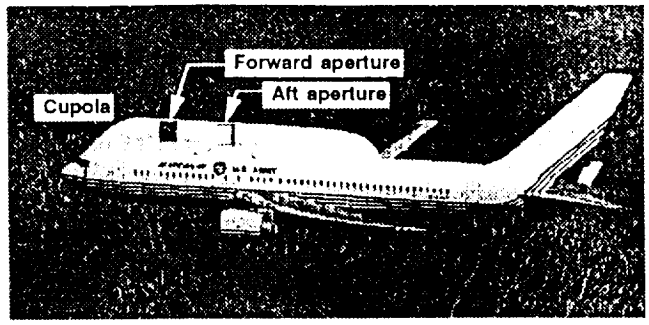

Fig. 7: U.S. Army Airborne Optical Adjunct

aperture. A characteristic inflow condition was used for the lip-blowing boundary, the flow rate computed using flight data and assuming isentropic compression of the ram air utilized in the aircraft. The 100% lip-blowing rate case corresponded to a $\dot{m} = 0.42(\rho u)_\infty$. For the discussion below, computed high and low lip-blowing rates refer to 100% and 1% of this mass flow rate. The coarsened near-field grids are shown in Fig. 8.

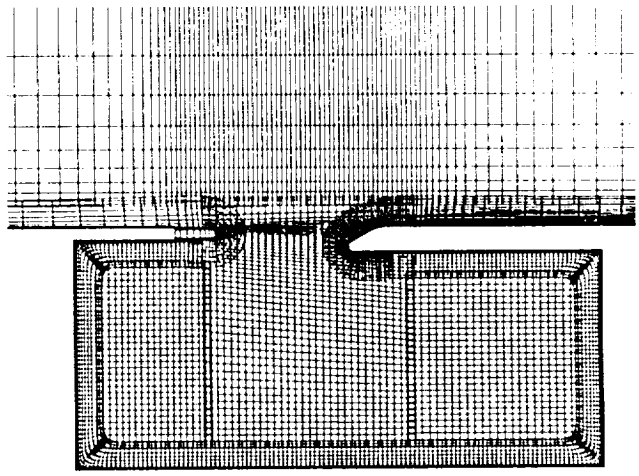

Fig. 8: 2-d treated cavity: near field grids

The mechanism by which an aft ramp reduces the cavity feedback was explained by Heller and Bliss.[20] Physically, this result can be explained from a force balance normal to a streamline approaching the stagnation point. About the stagnation point, the velocity gradient across the impinging shear layer creates a pressure gradient. However, there is a counteracting pressure gradient, $\rho q^2/r$, due to the differing radii of curvature above and below the dividing streamline.

For a rectangular cavity, the extreme of normal impingement of the shear layer onto the aft bulkhead causes further deflection into the cavity. Mass inges-

tion into the cavity causes increased pressure, deflecting the shear layer outwards. With the shear region now outwardly deflected, mass expulsion from the cavity reduces the cavity pressure, inducing another cycle. Therefore, between the extremes of a normal or tangential impingement of the shear layer, a balance of forces may be found. Use of a ramp instead of a convex surface at the reattachment region prevents shear layer perturbations from inducing instabilities of the type seen in rectangular cutouts. The length of the ramp must be large enough to accommodate the magnitude of the transverse shear layer excursions expected during operation.

Computed and flight mean Mach number profiles are compared in Fig. 9 for two lip-blowing rates. The quan-

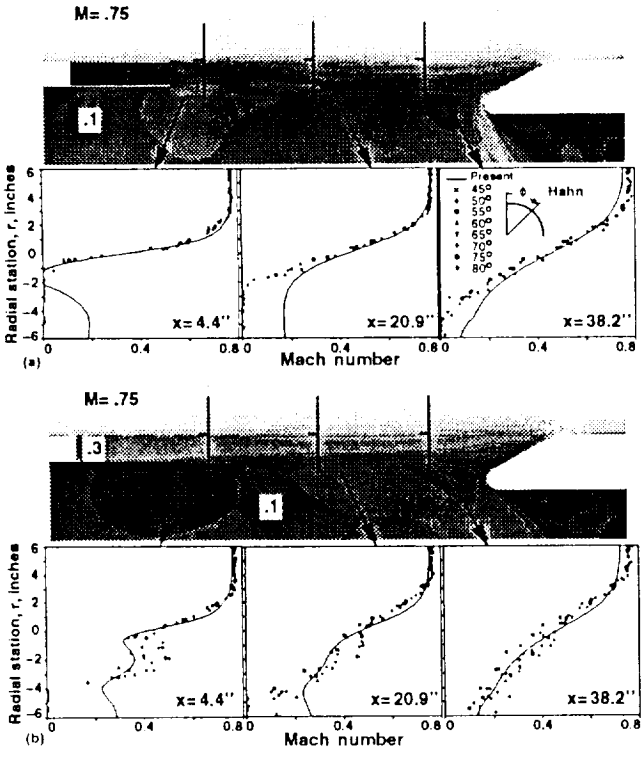

Fig. 9: 2-d treated cavity: instantaneous Mach number contours and mean profiles at (a) low and (b) high lip-blowing rate

tity ϕ indicates the angle from the cupola crest at which the data was measured. Figure 9 also shows Mach number contours for the two lip-blowing rates above each set of profiles. The Mach number contours are instantaneous while the profiles were averaged over 2000 time steps. The difference between experiment and computational results on the lower edge of the shear layer ($r < -2''$) may be due to the computational simplification of an empty cavity. The difference at the upper aft portion of the shear layer ($r > 2''$) appears to be due to blockage in the computational model. Overall, the maximum vorticity as a function of x-station is in agreement for both cases.

Comparisons of low lip-blowing rate power spectra at the aft ramp are shown in Fig. 10. The computed

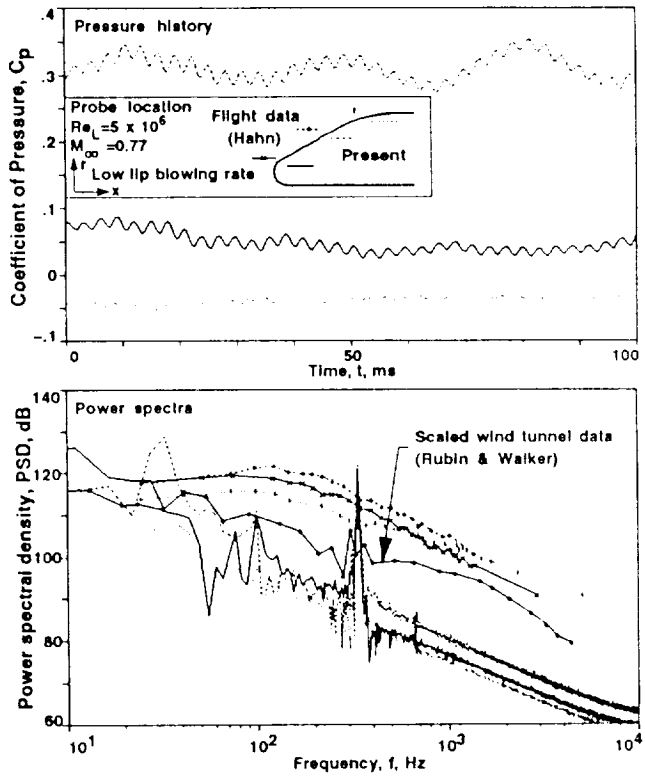

Fig. 10: 2-d treated cavity, low lip-blowing rate: power spectra

result generally falls 20 dB below the flight data, and a peak in the low lip-blowing rate spectra at 340 Hz is clearly computed, but is not seen in the flight data. Figure 10 also depicts data, the ordinate scaled by $\frac{q_\infty|_{flight}}{q_\infty|_{tunnel}}$ and the abcissa by $\frac{(c_\infty/L)_{flight}}{(c_\infty/L)_{tunnel}}$, obtained from an AOA wind tunnel test.[21] The data can be seen to agree more closely with the computed results than with flight data, and a small peak exists at the computed frequency peak. The computed high lip-blowing spectra was broadband, but generally underpredicted flight data.[19] Computed power spectra were found using 4096 points and a square window.

Experimental data[13, 22, 23, 24] indicates that the frequency of large structures in shear layers occurs at Strouhal numbers of $St = \frac{f\theta}{u_1+u_2} = 0.024 \pm 0.003$, where θ is the local shear layer momentum thickness and f de-

notes frequency. The computed Strouhal number can be estimated using Görtler's solution, given in Fig. 2a, to obtain $\theta = 0.036\frac{1-r}{1+r}x$ for $\sigma_0 = 11.0$, which is comparable to the empirically determined correlation[25] of $\theta = 0.034\frac{1-r}{1+r}x$. Specifying $r = 0.2$ in this relationship along with a compressibility correction,[26] the computed peak in the AOA solution at 340 Hz corresponds to a Strouhal number of 0.032. Note that by using Rossiter's formula, given in Fig. 5, the frequency obtained for $m = 5$ is 360 Hz. From Fig. 11 it can be seen that four vortical cycles exist ($m_v = 4$), implying that $m_a = m - m_v = 1$.

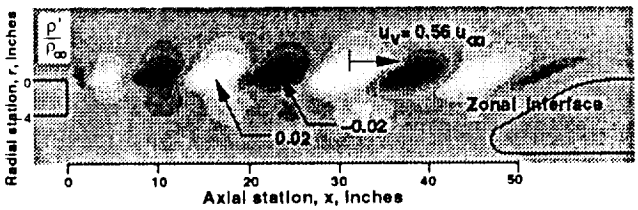

Fig. 11: 2-d treated cavity, low lip-blowing rate: instantaneous contours of $\frac{\rho'}{\rho_\infty}$

The cause of the spike in the power spectrum was found from inspection of density fluctuations, which revealed large convecting shear layer structures. Figure 11 shows a contour plot of $\frac{\rho'}{\rho_\infty}$, depicting the growth and propagation of the shear layer structures. The large structures, associated with a $0.03u_\infty$ vertical velocity component, are the primary contributors of the computed density fluctuations of the shear layer. The speed of the structures is $0.56u_\infty$,[19] below the value of $0.66u_\infty$ inferred by Rossiter for rectangular cutouts, yet above the $0.51u_\infty$ determined analytically by Roscoe and Hankey.[28]

Based upon these observations, it appears that large scale shear layer structures are being resolved. However, the lack of empirical support from the flight data pressure power spectra is at odds with this conclusion. Three-dimensional effects are a possible explanation for the discrepancy. Rockwell[27] noted that for sufficiently large Reynolds numbers three-dimensionality reduces coherence in the shear layer. This implies that assumption of two-dimensionality for small flow oscillations may be suspect. In this two-dimensional computation the mass removed from the cavity by the shear layer entrainment process can only be replenished at the impingement region. This is in contrast to the mass addition mechanism present in three-dimensions, which also includes mass replenishment via spanwise structures such as streamwise vortices. The evolution of streamwise-oriented vorticity interacting with the primary vortices would act to spread peaks in the reattachment ramp pressure spectra.

THREE-DIMENSIONAL RESONATING CAVITY

An experimental investigation of SOFIA cavity quieting treatments was performed in the NASA Ames $14' \times 14'$ wind tunnel in 1990.[7] The geometry shown in Fig. 12 was the initial cavity configuration tested in the wind tunnel. This simulation was implemented in order to demonstrate the capture of self-excited cavity resonance in three-dimensions. The simulated flow conditions were the same as used in the wind tunnel, with the flowfield initialized from a steady clean case. A stability-limited time step of $\Delta t = 3.53\mu s$ was used, corresponding to a streamwise $CFL \approx 1$ in the shear layer, and a $CFL|_{max} \approx 500$.

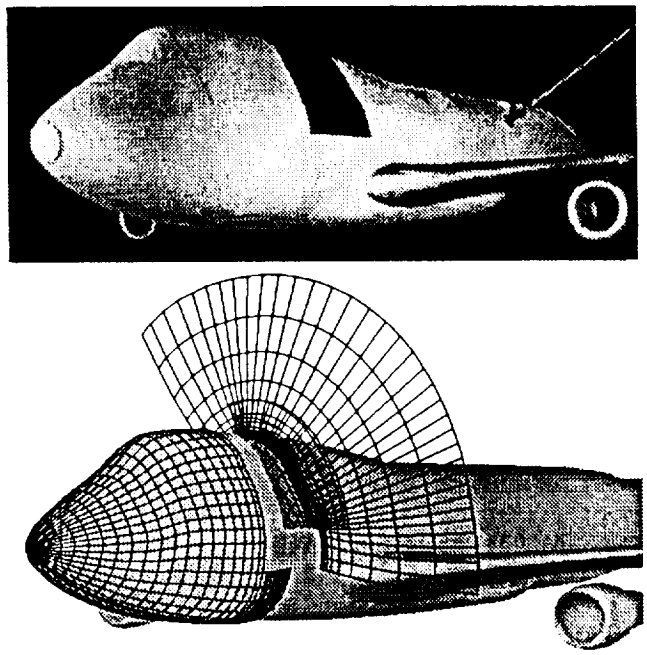

Fig. 12: Configuration 25: wind tunnel and numerical models

Sample pressure histories on the cavity walls and a comparison of the PSD resulting from the wind tunnel and numerical efforts are shown in Fig. 13. The PSD was obtained using 2048 points and a Hanning window to match the treatment of the experimental data. The predicted frequencies of the dominant tones appear reasonable, and the computed dominant tone is within 3 dB of experiment. The magnitudes of the computed higher modes are much lower than observed experimentally.

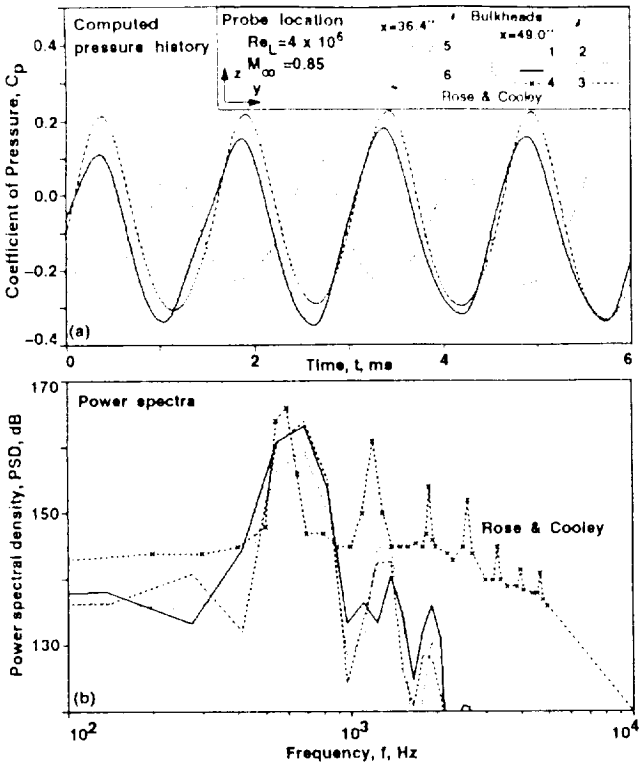

Fig. 13: Configuration 25: pressure histories and power spectra

Estimation of the grid resolution required to maintain a propagating wave of a specific magnitude can be deduced from the rectangular two-dimensional cavity and configuration 25 results. First, wavelength can be estimated by assuming the wave to be harmonic at a given frequency and travelling at the stagnation speed of sound. Next, it is noted that frequencies around 2 kHz were resolved well in the two-dimensional case, in which the grid resolution was such that about 40 points supported the wave. From the configuration 25 results, it is seen that only the 700 Hz peak is well resolved, which again gives approximately 40 points across the wave for this coarser grid. Although numerical damping of the higher frequencies can be expected, most of the energy is contained in the lowest frequency mode, as can be seen in the sound pressure level, or SPL, comparison of Fig. 14. Figure 14 also shows a quieted configuration which is discussed below.

THREE-DIMENSIONAL QUIETED CAVITY

During the wind tunnel experiments, use of a blended aft ramp resulted in the lowest sound production levels. This simulation was implemented in order to determine

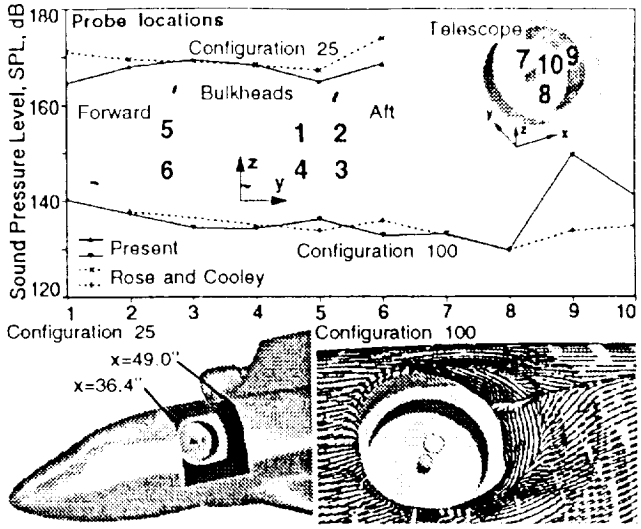

Fig. 14: Comparison of sound pressure levels

if the same level of quieting could be predicted numerically as was observed experimentally. Figure 15 shows the topology of the blended aft ramp grids used in this simulation of configuration 100.

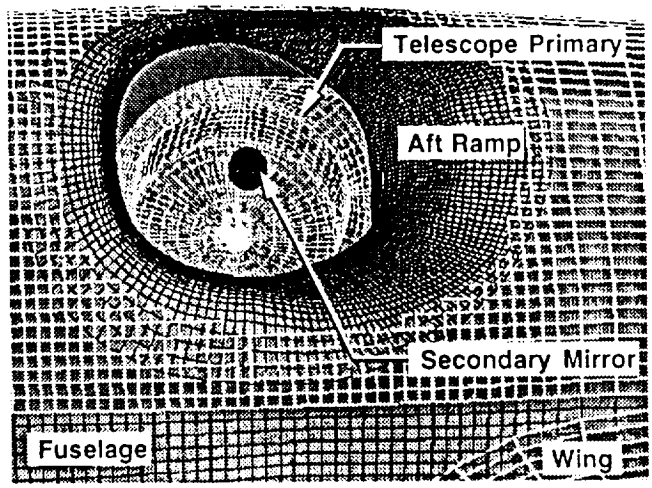

Fig. 15: Configuration 100: cavity region topology

For the SOFIA experiment, this type of geometry treatment was found to be quieter than the untreated configuration 25 case by over 30 dB. Figure 14 summarizes that the proper trends were computed. The flow conditions were again initialized from a clean case, and integrated using a stability-limited time step size of $\Delta t = 7.06 \mu s$. The frequency domain analysis was obtained using 4096 points, a Hanning window, and no zero-padding.

A qualitative comparison of results can be made from inspection of the computed instantaneous streamlines depicted in Fig. 14 and the oil flow from a similar molded geometry, shown in Fig. 16. A strong cross flow component is evident at the aft ramp for this aperture elevation angle, and is seen computationally as well.

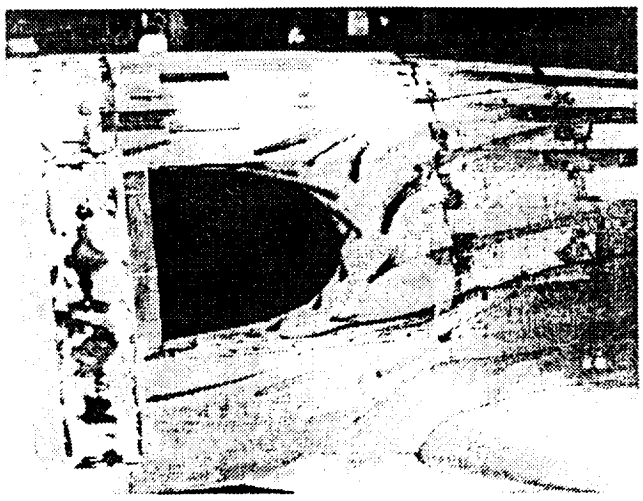

Fig. 16: Experimentally[7] observed surface flow pattern

Quantitative comparisons were made for this passively quieted cavity geometry in terms of shear layer profiles and pressure spectra in the cavity. Since errors in shear layer mass entrainment rate would adversely affect the cavity velocity field and hence the mean telescope loads, an important validation parameter is the shear layer spread rate. Figure 17 depicts mean experimental and computational shear layer Mach number profiles. The vertical scale of the profiles is twice that shown in the contour plot for clarity. Note that the experimental profiles were obtained using a rake, which is sensitive only to u, the x-component of velocity. Figure 17 indicates reasonable agreement in profile shape, however the computed growth rate is lower than seen in the data. This discrepancy may be due to geometry modifications in the experiment or specification of an overly-large value of σ_0.

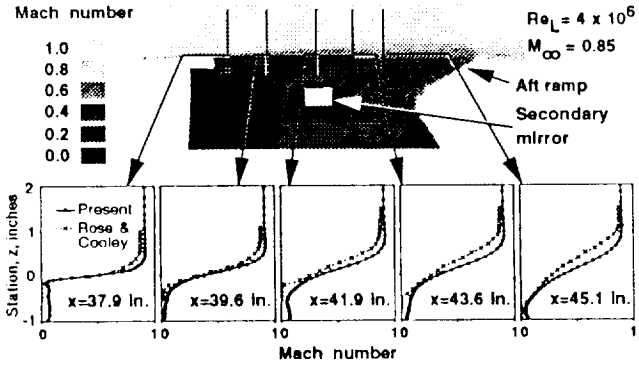

Fig. 17: Configuration 100: instantaneous Mach number contours and mean profiles

Assessment of the oscillating telescope assembly loads requires the accurate resolution of the unsteady pressure field in the cavity. Comparison of the computed and observed spectra at specific locations provides a measure of confidence for the computed telescope loads. Toward the estimation of loads, Fig. 18 shows the pressure history and resultant PSD on the cavity walls. Although the peak levels are in agreement, the computed spectra can again be seen to drop more rapidly with frequency than the experimental results due to numerical dissipation. The spectral peak at 1800 Hz corresponds to a Strouhal number of 0.027, using a velocity ratio of 0.1.

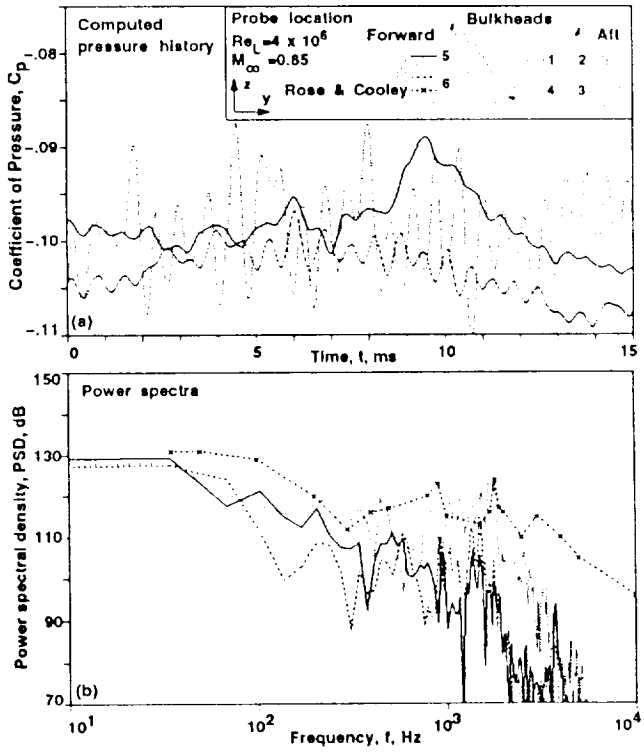

Fig. 18: Configuration 100: pressure history and power spectra on cavity wall

THREE-DIMENSIONAL QUIETED AFT CAVITY

Recently a new configuration which places the cavity aft of the wing, as shown in Figs. 19 and 20, has been proposed as a cost-effective configuration. However the cavity response of this aft telescope installation is of

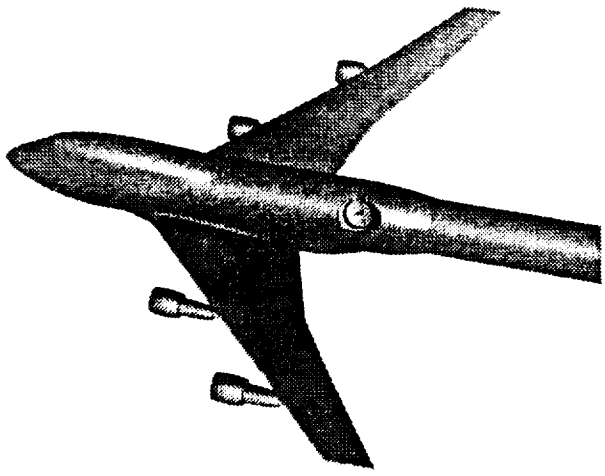

Fig. 19: Aft telescope configuration: modelled geometry

concern. Limited wind tunnel access has prevented timely resolution of this safety issue through experimental testing, hence this computation will provide an early measure of performance. Flight conditions at 41,000 feet and $M_\infty = 0.85$ were used, resulting in a $Re_L = 2.3 \times 10^7$. Powered engines were simulated by specification of characteristic conditions for the inlets and both fan and core exhaust nozzles. The tail geometry was not available for this simulation.

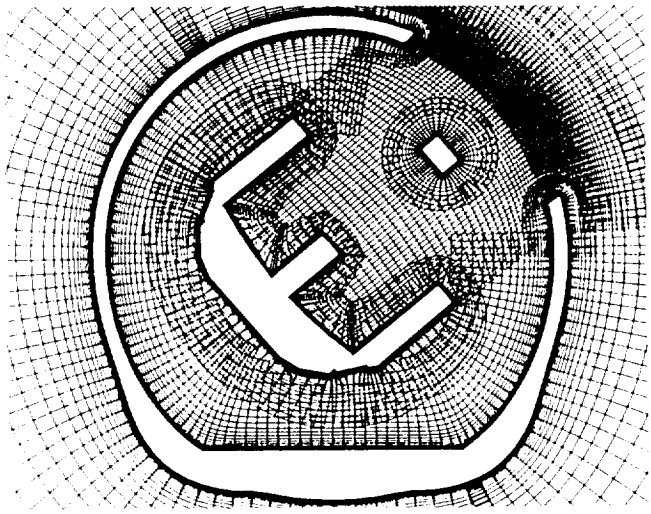

Fig. 20: Aft telescope configuration: cavity grids

As with the forward cavity computations, a clean aircraft flowfield was used as an initial condition for the cavity computation. Figure 21 compares the computed pressure coefficient profiles along the crest, side, and bottom of the model with flight data,[29] where the cavity location is shown for reference. Computed pressures are generally in agreement with the data, but the computed gradient aft of the cavity location is more adverse than seen in the flight data. This is probably due to discrepancies in the empennage geometry and the lack of tail stabilizers.

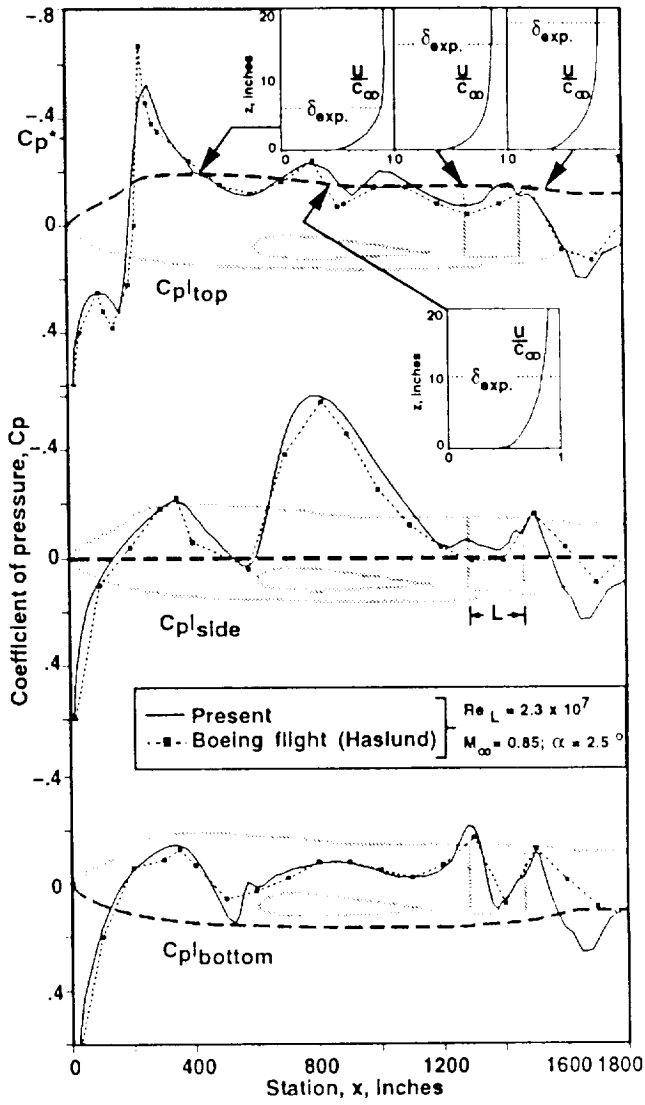

Fig. 21: Clean configuration: pressure coefficient comparison

Figure 22 shows the computed PSD on the aft ramp as compared to the scaled forward cavity wind tunnel data. The spectra was computed using 1024 points stored at $5\Delta t \approx 0.68\ ms$ intervals. The computed and scaled experimental spectra can be seen to be similar in shape and magnitude to about 100 Hz, where numerical dissipation becomes significant. The cavity grid cells,

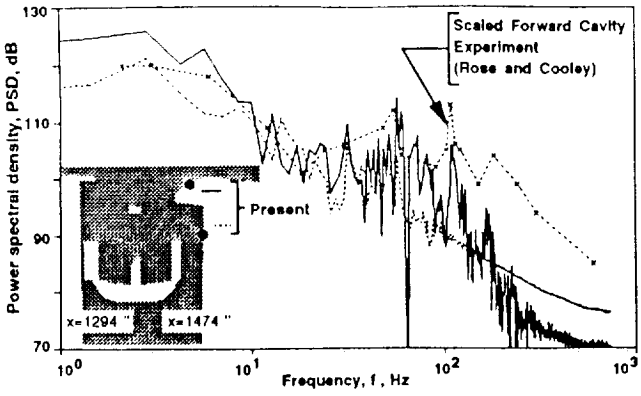

Fig. 22: Aft telescope configuration: power spectra

approximately 3 *in.* on a side, had been sized so that only low frequencies were well resolved. Use of smaller cells would capture short wavelength, high frequency waves which are unable to excite the massive telescope assembly. A Strouhal number of 0.028 is computed for the spectral peak seen at 110 Hz.

Simulation of the distortion of a planar wavetrain of light propagating through the cavity aperture[19] reveals the presence of convecting structures, shown in Fig. 23. The wavefront distortion, or optical path difference (OPD), is proportional to the integrated density normal to the aperture. Using $f_v = \frac{u_\infty}{\lambda_v}$ and Fig. 23, it can be verified that the $St = 0.028$ peak is caused by the resolved shear layer structures. The structures convect with the local downwash velocity field caused by the wing. A large spanwise variation of the wavefront distortion can also be seen, with maximum $< OPD' >$ values at the crossflow edges of the aperture. Since the shear layer grid is uniformly distributed in this region, this spanwise variation may be indicative of increased vortex coherence at the boundaries of the aperture.

CONCLUSIONS

The development of an aerodynamic configuration analysis method has been summarized. The topology used within the overset framework has allowed simple and fast mesh generation while maintaining high resolution in critical flow regions.

Evaluation of the overset mesh method was performed through comparison against experiment for several related flows. Sound pressure levels for resonant and quieted cavities compared well with experiment. However, use of a planar flow assumption for a quieted cavity appears to have caused a computed spectral peak where flight data indicated broadband behavior. Computed shear layer structures were found to cause the

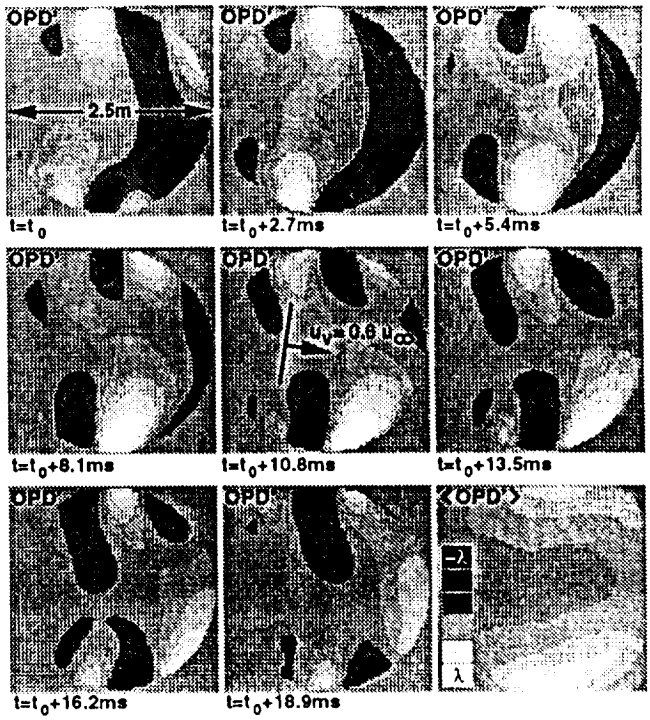

Fig. 23: Aft telescope configuration: wavefront distortion

spectral peak at a Strouhal number of approximately 0.03. In three-dimensions, a similar peak was seen in both experiment and simulation. Additionally, large spanwise density variation of the aperture structures was found.

REFERENCES

[1] Cameron, R.M., Bader, M., and Mobley, R.E., "Design and Operation of the NASA 91.5-cm Airborne Telescope," *Applied Optics,* Vol. 10, Sep. 1971, pp. 2011-2015.

[2] Atwood, C.A., and Van Dalsem, W.R., "Flowfield Simulation about the SOFIA Airborne Observatory," AIAA-92-0656, Jan. 1992. Accepted to the *AIAA J. of Aircraft.*

[3] Birch, S.F. and Eggers, J.M., "A Critical Review of the Experimental Data for Developed Free Turbulent Shear Layers," *Free Turbulent Shear Flows,* NASA SP-321, July 1972.

[4] Driver, D.M., and Seegmiller, H.L., "Features of a Reattaching Turbulent Shear Layer in Divergent Channel Flow," *AIAA J.*, Vol. 23, Feb. 1985, pp. 163-171.

[5] Rossiter, J.E., "Wind-Tunnel Experiments on the Flow Over Rectangular Cavities at Subsonic and Transonic Speeds," Royal Aircraft Establishment Reports and Memoranda No. 3438, Oct. 1964.

[6] Hahn, M.M., "Flight Test Verification of the Aerodynamic Characteristics of the 767-AOA Open Viewports," Boeing Commercial Airplane Company, Doc. D041T207TN, Fall 1987.

[7] Rose, W.C. and Cooley, J.M., "SOFIA Wind Tunnel Data Analysis and Implications for the Full-Scale Aircraft," Rose Eng. and Research, Inc., Dec. 1990.

[8] Pulliam, T.H. and Chaussee, D.S., "A Diagonal Form of an Implicit Approximate-Factorization Algorithm," *J. Comp. Phys.*, Vol. 39, Feb. 1981, pp. 347-363.

[9] Benek, J.A., Buning, P.G., and Steger, J.L., "A 3-D Chimera Grid Embedding Technique," AIAA-85-1523, July 1985.

[10] Baldwin, B.S. and Lomax, H., "Thin-Layer Approximation and Algebraic Model for Separated Turbulent Flows," AIAA-78-257, Jan. 1978.

[11] Buning, P.G. and Chan, W.M., "OVERFLOW/F3D User's Manual, Version 1.5," NASA/ARC, Nov. 1990.

[12] Liepmann, H.W. and Laufer, J., "Investigations of Free Turbulent Mixing," NACA TN-1257, 1947.

[13] Brown, G.L. and Roshko, A., "On density effects and large structure in turbulent mixing layers," *J. Fluid Mech.*, Vol. 64, Part 4, 1974, pp. 775-816.

[14] Chan, W.M. and Steger, J.L., "Enhancements of a Three-Dimensional Hyperbolic Grid Generation Scheme," *App. Math. and Comp.*, Vol. 51, pp. 181-205.

[15] Steinbrenner, J.P., Chawner, J.R., and Fouts, C.L., "A Structured Approach to Interactive Multiple Block Grid Generation," AGARD FDP Specialists Mtg. on Mesh Generation for Complex Three-Dimensional Configurations, Loen, Norway, May 1989.

[16] Karamcheti, K., "Acoustic Radiation from Two-Dimensional Rectangular Cutouts in Aerodynamic Surfaces," NACA TN-3487, 1955.

[17] Rockwell, D. and Naudascher, E., "Review – Self-Sustaining Oscillations of Flow Past Cavities," *Transactions of the ASME*, 100, June 1978, pp. 152-165.

[18] Om, D., "Navier-Stokes Simulation for Flow Past an Open Cavity," *AIAA J. of Aircraft*, Vol. 25, Sep. 1988, pp. 842-848.

[19] Atwood, C.A., "Navier-Stokes Simulations of Unsteady Transonic Flow Phenomena," NASA TM-103962, Aug. 1992.

[20] Heller, H.H. and Bliss, D.B., "Aerodynamically Induced Pressure Oscillations in Cavities - Physical Mechanisms and Suppression Concepts," AFFDL-TR-74-133, Feb. 1975.

[21] Rubin, D.V. and Walker, B.J., "AOA Aero-Optical Wind Tunnel Test Final Analysis Report," Technical Report RD-SS-86-8, U.S. Army Missile Command, Feb. 1986.

[22] Hussain, A.K.M.F. and Zaman, K.B.M.Q., "An experimental study of organized motions in the turbulent plane mixing layer," *J. Fluid Mech.*, Vol. 159, 1985, pp. 85-104.

[23] Oster, D. and Wygnanski, I., "The forced mixing layer between parallel streams," *J. Fluid Mech.*, Vol. 123, 1982, pp. 91-130.

[24] Winant, C.D. and Browand, F.K., "Vortex pairing: the mechanism of turbulent mixing-layer growth at moderate Reynolds number," *J. Fluid Mech.*, Vol. 63, 1974, pp. 237-255.

[25] Roberts, F.A. and Roshko, A., "Effects of Periodic Forcing on Mixing in Turbulent Shear Layers and Wakes," AIAA-85-0570, Mar. 1985.

[26] Bogdanoff, D.W., "Compressibility Effects in Turbulent Shear Layers," *AIAA J.*, Vol. 21, June 1983, pp. 926-927.

[27] Rockwell, D., "Oscillations of Impinging Shear Layers," AIAA-82-0047, Jan. 1982.

[28] Roscoe, D.F. and Hankey, W.L., "The Stability of a Compressible Free Shear Layer," AFWAL-TR-80-3016, Oct. 1979.

[29] Haslund, R.L., "SOFIA Viewport Configuration Wind Tunnel Test Report," Boeing Aerospace and Electronics Sensors Technology, Oct. 1988.

APPENDIX D